Full Length Article

Soot structure and flow characteristics in turbulent non-premixed methane flames stabilised on a bluff-body

Amir Rowhani [a,*], Zhiwei Sun [a], Alfonso Chinnici [a], Paul R. Medwell [a], Graham J. Nathan [a], Bassam B. Dally [b]

[a] School of Mechanical Engineering, The University of Adelaide, South Australia 5005, Australia
[b] Clean Combustion Research Centre (CCRC), King Abdullah University of Science and Technology (KAUST), Thuwal 23955-6900, Saudi Arabia

ARTICLE INFO

ABSTRACT

The soot properties of methane in turbulent regimes are not well characterised but are highly desirable. Methane is the main constituent of natural gas that is broadly used in many industrial combustors. Investigation of turbulent methane flames under well-defined boundary conditions is therefore useful for interpreting soot formation in practical burners and can be used for further model development. This study presents a joint experimental and numerical study of a series of turbulent non-premixed bluff-body flames fuelled with pure methane for three values of the momentum flux ratio of fuel jet to co-flowing air. Soot volume fraction (*SVF*) and flowfield are measured simultaneously using planar laser-induced incandescence (P-LII) and 2D-polarised particle image velocimetry (P-PIV). Additionally, time-averaged temperature, mixture fraction, OH and C_2H_2 concentrations are estimated numerically using RANS models. The global flame structure for all three flames features a recirculation zone with a double-vortex structure, a jet-propagating zone, and a neck zone connecting the two regions. The soot distribution within the recirculation zone shows clear distinct features, which is attributed to the mean mixture fraction distribution in this zone. Increasing the momentum flux ratio shifts the location of the mean stoichiometric mixture fraction to the rich inner vortex core, leading to a distinct peak of the total integrated soot in the inner vortex of the recirculation zone that is not observed in other cases. Also, it is deduced that the soot inception starts earlier in the recirculation zone for the flame with the highest momentum flux ratio and in the jet zone for the other two flames. Much higher soot concentration and lower intermittency are found with ethylene-based flames stabilised on the same burner and with the same operating conditions. In addition, the study has generated a database of soot and flowfield results, which can be helpful for future model validations.

1. Introduction

Research into the control of soot formation and the mitigation of its emission from flames has been ongoing for decades due to ever-increasing environmental and health concerns. The primary fuel used in most of these studies is ethylene due to its high soot propensity as the simplest alkene and the relatively simple chemistry, which is desirable for modelling purposes. Consequently, a detailed understanding of ethylene combustion kinetics and soot formation and oxidation mechanisms have been developed over the years [1–3]. On the other hand, natural gas, which mainly contains methane, is widely used in domestic and industrial applications, such as gas turbines, furnaces, and kilns. The use of natural gas as a transitional fuel to replace other fossil-based fuels, such as coal and HFO, has increased over the last two decades. Natural

gas is projected to be the strongest-growing fossil fuel with more than 200 million metric tons of new capacity required by 2050 [4]. Hence, further research into the combustion of methane and its emission characteristics (soot in particular) under practical operating conditions is warranted.

It is well known that the molecular structure of the fuels plays a significant role in the onset of soot formation [5,6]. In non-premixed mode, the sooting tendency for alkenes is higher than alkanes. The differences between soot formation in C1 and C2 fuels stem from the makeup of the radical pool, acetylene concentrations, and PAH formation pathways [7–10]. In the laminar regime, methane is only slightly sooting at atmospheric pressure. However, increasing the pressure (up to 60 bar) accelerates the PAH condensation rate followed by acetylene addition, which enhances soot by a factor of five to six [11–13]. In

methane flames, inception is reported to be the dominant mechanism [14] while in ethylene flames, the inception phase is relatively short, and the surface growth and agglomeration dominate the soot formation mechanism [15]. Additionally, the C_2H_2 contribution to soot surface growth mechanism is found to be higher in C_2H_4 when compared to CH_4 [16]. Such differences result in additional difficulties in predicting soot in methane-based flames where the inception mechanism is poorly understood. In this context, flames with well-defined initial and boundary conditions and sufficiently long residence time, favouring soot inception, are needed to better understand the formation of alkanes-based flames. Bluff-body flames offer such conditions and hence are the target of this study.

Several groups have investigated the soot-flowfield interaction to quantify the mixing effects using different fuels and under turbulent flames' conditions. Global correlations have been established for a range of turbulent flames, including simple jets [17–24], bluff-body [25,26], and swirling burners relevant to gas turbines [27]. These global parameters are characterised mainly by the global fuel exit strain rate, U/D_J, and the global mixing rate, defined as the inverse of the residence time, $1/\tau_G$. Mahmoud et al. [19–21] reported a linear correlation between the exit strain rate and the global mixing rate in momentum-dominated jet flames fuelled with ethylene, nitrogen and hydrogen fuel mixture. Qamar et al. [17,18] investigated natural gas combustion in the turbulent regime and provided detailed correlations between the global mixing rate and soot formation for different burner geometries. Other flames, including swirl-stabilised flames, were also investigated using ethylene [27,28] and Jet A-1 [29] fuels to provide further insight into the soot-flowfield interactions in flames with the recirculating flow. Our study on bluff-body turbulent flames fuelled by ethylene-nitrogen mixture has shown that there are no clear correlations between the local instantaneous *SVF* and strain rate within the recirculation zone and the bluff-body flames' jet region, which suggests that the time-scales for *SVF* are significantly greater than those driving local fluctuations [30,31]. While these studies provide an insightful understanding of the soot-flowfield interactions for flames fuelled with ethylene, there are only limited similar studies for methane flames.

Therefore, the objectives of the current study are: (a) to investigate the soot formation and destruction of a series of turbulent non-premixed pure methane flames on an axisymmetric bluff body burner, and to assess the dependency of sooting characteristics on flowfield, temperature, and mixture reaction distribution; (b) to investigate the effect of momentum flux ratio of the fuel jet and co-flowing air on the soot distribution along the entire length of the methane flames; and (c) to provide a unique high fidelity experimental data that can be used for further model validations.

2. Experimental setup

2.1. Bluff-body burner

An axisymmetric bluff-body burner that has been employed in earlier work [30–32], with a fixed outer diameter of 64 mm, was used in this experimental campaign. With a central jet diameter of 4.6 mm, the capped brass tube is surrounded by a co-flowing air stream introduced through a round cross-section air contractor with an inner diameter of 190 mm. The round contractor helps avoid the formation of corner vortices that occur in square cross-section contractions. To allow optical access, the bluff-body was mounted 10 mm above the exit plane of the air contractor. The burner tunnel assembly was translated vertically, using an electrically powered traverse to measure the entire flame length. A large extraction hood (800 mm diameter) was also traversed with the burner tunnel assembly, such that a fixed distance of 300 mm from the flame tip to the hood inlet was kept, and where the hot combustion products were extracted. This arrangement reduces any effect from the exhaust hood on the flame as the burner and contraction assembly are traversed vertically.

2.2. Flow conditions

Table 1 shows a summary of the flow parameters investigated in this study. Methane, with a purity of 99.99%, was used as fuel. The co-flowing air and the fuel were at ambient temperature and atmospheric pressure. The resulting flames are labelled as MB series flames, where M and B stand for methane and bluff-body. The fuel flow rate was set to 0.32 g/s for the MB-1 flame, giving a bulk mean exit Reynolds number, based on the jet inner diameter, of 8,000, while the coflow air velocity was set to 14.1 m/s. The Reynolds number for flames MB-2 and MB-3 was increased to 15,000 (methane flow rate of 0.61 g/s) while the coflow was set to 14.1 and 20 m/s, respectively. The increase in the coflow air velocity aims to investigate the effect of mixture strength in the recirculation zone corresponding to the reduction in momentum flux ratio of jet to coflow [32,33], defined as, $G = (\rho U^2)_{Fuel}/(\rho U^2)_{Air}$.

2.3. LII and PIV setup

The diagnostic system is identical to earlier research and the details can be found in the publications by the same authors [30]. A schematic of the experimental apparatus is also shown in Fig. 1. In brief, the apparatus comprises planar laser-induced incandescence, P-LII, aligned with a 2D-polarised particle image velocimetry system. A pulsed Nd: YAG laser (Q-smart 850, Quantel) with the fundamental output (1064 nm) operating at 10 Hz is used for the P-LII measurements. The incandescence from soot particles was collected through an intensified (ICCD) camera through a 430 nm (10 nm bandwidth) filter to suppress interference from the C_2 laser-induced emissions and flame radiation [32]. The gate width of the LII camera was set to 50 ns with prompt timing relative to the LII excitation. The LII beam was formed into a sheet by passing it through the sheet-forming lenses, with the dimensions of 0.5 mm $\times$ 70 mm. The LII laser fluence was kept above 0.5 J/cm^2, in the plateau region of the LII response curve to minimise the laser energy variation effects from the beam steering and attenuation on the resulting LII signals [33]. One thousand LII images were collected and converted to soot volume fraction (*SVF*) by calibration against one of the flat premixed McKenna target flames ($\Phi = 2.34$) from the International Sooting Flame Workshop (ISF) [34]. A 1064-nm continuous-wave (CW) diode-pumped-solid-state laser (DPSS) was utilised to perform the laser extinction calibration measurements in the McKenna target flames. The minimum detection limit in the collected data was determined to be 1 ppb. The details of the calibration were reported previously [19,20]. The P-LII data was only extracted from the core of the images due to the signal variation in the upper and lower sides of the laser sheet. A standard deviation of 13% was observed in P-LII data extracted from the laminar McKenna burner flame. Also, the data was only processed on the beam entrance side of the flame to avoid beam steering effects. Sun et al. [35] reported a 2 mrad and consequently 50% increase in the laser sheet width and 750 μm out-of-plane direction throughout the flame. Signal trapping has been previously quantified in a series of ethylene flames and is considered negligible. Since the soot concentration in the methane flames is significantly lower than the ethylene counterparts, the signal trapping is assumed to be minor [36].

The PIV measurements were performed using a 10 Hz pulsed dual-head Nd:YAG laser (Quantel BrilliantB/Twins) frequency-doubled (532 nm). The PIV pulses were offset by 10 μs to 60 μs, depending on the exit jet and co-flow velocities. The Mie scattering from the 1-μm titanium oxide (TiO$_2$) seeding particles was collected using a CCD Kodak Megaplus II camera (1920 $\times$ 1080 pixels^2, 16 bit), equipped with a Sigma lens (105 mm, f = 2.8). Two additional polarisers to a conventional PIV system were utilised to significantly suppress the scattered interference from soot particles [31,37]. One-micron titanium oxide (TiO$_2$) particles were injected into the flow through an in-house built fluidised-bed particle seed generator in both the jet and the co-flow streams. The Mie scattering from the TiO$_2$ particles was captured with a CCD camera (Kodak Megaplus II, 1920 $\times$ 1080 pixels^2) equipped with

Table 1

Summary of the flow conditions for a series of pure methane (99.99% CH_4) flames stabilised on a bluff-body burner with the jet and bluff-body diameters of 4.6 mm and 64 mm, respectively.

Flame case	U_J (m/s)	Re_J (-)	$\dot{m}_f$ (g/s)	Q_{LHV} (kW)	U_C (m/s)	$\overline{L}_{RZ}$ (mm)(±5%)	$\overline{L}_f$ (mm)(±5%)	G (-)
MB-1	31.8	8,000	0.34	17	14.1	91.3	736	2.63
MB-2	59.6	15,000	0.61	30.5	14.1	105.1	928	9.21
MB-3	59.6	15,000	0.61	30.5	20	98.8	806	4.57

G –momentum flux ratio; $\overline{L}_{RZ}$ – Mean recirculation zone length; $\overline{L}_f$ – Mean visible flame length; $\dot{m}_f$ – Fuel flow rate; Q_{LHV}– Heat input by fuel; Re_J – Jet exit Reynold; U_C – Bulk co-flowing air velocity; U_J – Bulk jet exit velocity.
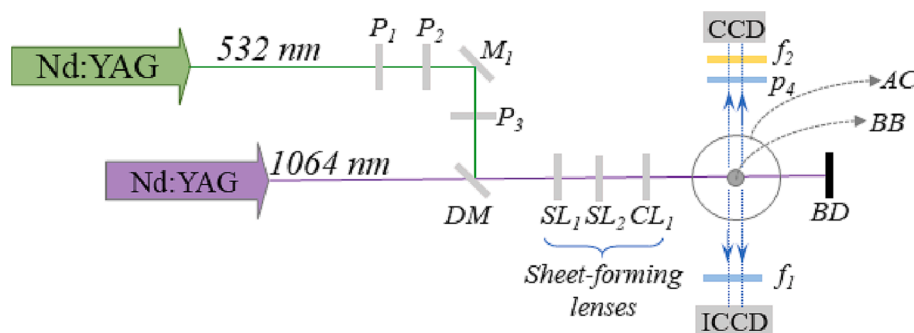
Fig. 1. Experimental layout adopted from earlier work [30]. (AC – Air contractor; BB – Bluff-body burner; BD – Beam dump; CCD – Charged-coupled device; CL_1 – Cylindrical lens; DM – Dichroic mirror; f_1 – 430 nm filter; f_2 – 532 nm bandpass filter; ICCD – Intensified charged-coupled device; M_1 – 532 nm mirror; P_1 – $\lambda/2$ wave plate; P_2 – 532 nm film polariser; P_3 – Linear polariser; P_4 – linear polariser and SL_1/ SL_2 – Spherical lenses).

a Sigma lens 105 mm, f-number 2.8. A 532 nm bandpass filter (Andover) with an FWHM of 1 nm was fitted to the camera lens to suppress laser-induced incandescence. One thousand PIV image pairs were recorded and processed using commercial software, PIVLab 2.20 [38,39]. Background noise was removed from raw images in the post-processing step. The interrogation window was sequentially reduced from 64 × 64 to 32 × 32, and ultimately to 16 × 16 pixels^2 with 50% overlap, to provide a minimum spatial resolution of 1.48 × 1.48 mm^2. The total error of the PIV measurements was estimated to be ± 1.16 m/s [32].

2.4. Numerical model

The CFD method was used in this work to assist in better interpreting the observed trends using the same model from our earlier work [32]. The MB-1, MB-2, and MB-3 flames were modelled using ANSYS Fluent 21 R1 [40]. A 2-D axisymmetric model of the bluff-body burner was developed, with a fuel jet in the centre surrounded by concentric coflow air. Following a mesh-independence study, a structured mesh with 610,000 cells was generated [27]. The governing equations for mass, momentum and energy were solved using steady, incompressible Reynolds-averaged Navier − Stokes (RANS) equations. The standard k-ε model with modified coefficients [41,42] was selected for turbulence closures. The steady flamelet model, coupled with the DRM-22 reduced kinetic mechanism (22 species and 104 reactions), was used for the combustion model. The radiative heat transfer was calculated with the discrete ordinates method (DO). The COUPLED algorithm was employed to solve the flowfield, with second-order spatial discretisation for all variables. The CFD was validated against the current velocity measurements with a very good agreement (<4% differences). To validate the model, a comparison of the predicted and measured mixture fraction, temperature, and velocity components have been performed in a similar version of non-sooting bluff-body flames. Additionally, the current work's measured axial and radial velocity components have been compared with the calculated values. The supplementary material (Fig. S1 and Fig. S2) presents the validation data.

3. Results and discussion

3.1. Global flame structure

The global appearance of the three methane flames stabilised on the bluff-body burner, shown in Fig. 2, is similar to previously studied non-premixed bluff-body flames [25,32,41–43]. Regardless of the fuel type, these flames typically feature an upstream recirculation zone close to the bluff-body surface, a jet-propagation region further downstream, and an almost soot-free neck zone connecting these two regions. The blue length of the region above the recirculation zone increases with both the increase in the jet (MB-2) and co-flow (MB-3) velocities, where MB-3 shows the longest neck region. The neck zone is characterised by a high strain rate, enhanced mixing with the coflowing air and the hot products from the recirculation zone, and a central fuel stream [43]. The mean flame visible length ($\overline{L}_f$), which is estimated from 10 binarized instantaneous flame images, is found to be 736 mm, 928 mm, and 806 mm for MB-1, MB-2, and MB-3 flames, respectively. The total averaged flame length is linked to the momentum flux ratio of the flames. Increasing the fuel velocity from 31.8 m/s in MB-1 flame to 59.6 m/s and keeping the coflowing air velocity at 14.1 m/s resulted in the highest flame length since the excess fuel is transported to the jet region. In MB-3, on the other hand, increasing the coflow air velocity to 20 m/s in MB-3 flame helps induce more fuel into the recirculation zone, reducing the amount of fuel reaching the rest of the flame, and leading to a reduction in the overall length by 13%, as compared with MB-2.

The momentum flux ratio (G), defined as $G = (\rho U^2)_{Fuel}/(\rho U^2)_{Air}$ is calculated for the three flames and presented in Table 1. This ratio is found to be 2.63, 9.21, and 4.57 for the MB-1, MB-2, and MB-3 flames, respectively. Dally et al. [42] showed that for a series of flames operating with various fuels, including H_2, CNG, LPG, and C_2H_4, the transitional momentum flux ratio between the single and double vortex structure in the bluff-body flames happens at G between 13 and 15. Consistent with this, the momentum flux ratio calculated for these flames is below the transition threshold to a single vortex flame. Hence, all three flames include two vortices, an inner and an outer vortex within
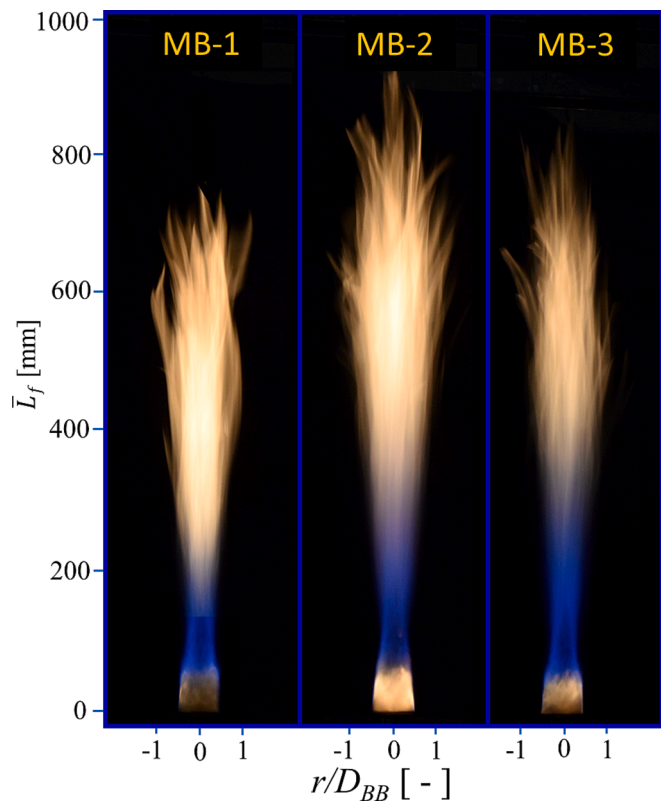
Fig. 2. Photographs of the pure methane flames stabilised on the bluff-body burner; MB-1 (left), MB-2 (middle), and MB-3 (right).

the recirculation zone. The correlations between the momentum flux ratio (G) and both the mean flame length ($\bar{L}_f$) and total soot volume in the recirculation zone (SV_{RZ}) are presented in Fig. 3. Here, SV_{RZ} represents the volume-integrated SVF in m³ in the recirculation zone and is obtained using the following expression

$$SV_{RZ} = 2\pi r \int_0^{x_{max}} \int_0^{r_{max}} SVF(r,x)\, dr.dx \tag{1}$$

where $SVF(r,x)$ is the local soot volume fraction at a certain height above the burner, x, and a radial distance from the axis, r. For the recirculation zone, the parameter x_{max} is set to the length of the recirculation zone (L_{RZ}), as defined in Section 3.2. The dependence of both mean flame length and the total soot volume in the recirculation zone on the momentum flux ratio can be reasonably characterised with exponential fits for the present flames. It is notable too that more data points
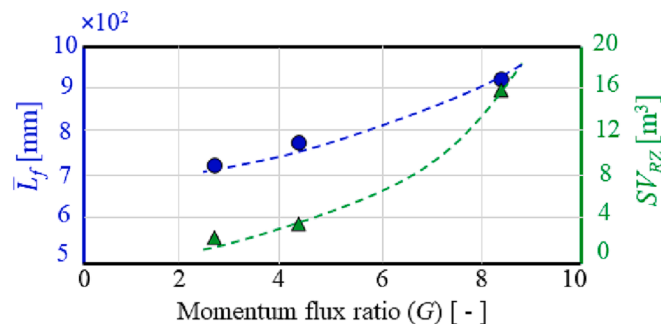

Fig. 3. The mean total flame length ($\bar{L}_f$) in blue and total soot volume in the recirculation zone (SV_{RZ}) in green, plotted as a function of momentum flux ratio, G. The symbols present the measured data and the dashed-lines show the best exponential fits. (For interpretation of the references to colour in this figure legend, the reader is referred to the web version of this article.)

are needed to establish a more generic correlation for these flames, and the current fit appears plausible for the range of conditions considered in this work.

3.2. Time-averaged flowfield features

The mean flowfield features for the three flames were calculated from 1000 instantaneous image pairs obtained from the PIV measurements. Fig. 4 presents the typical mean vector field overlaid on the mean velocity and mean shear strain rate for MB-1 flame, as a reference flame, at axial locations up to $x/D_{BB} = 2.0$. The 2D shear-strain rate, S_{rx}, has been calculated from the velocity components obtained from the PIV, using the following formula:

$$|S_{rx}| = \frac{1}{2}\left|\left(\frac{\partial u}{\partial x} + \frac{\partial v}{\partial r}\right)\right| \tag{2}$$

where u and v are the axial and radial velocity components, respectively. The strain rate is the magnitude of averaged strain rate calculated from the PIV data. Since all three flames exhibit similar characteristics within the recirculation zone, namely two vortices between the inner and outer shear layers, only the MB-2 flame is represented in Fig. 4.

The length of the recirculation zone (L_{RZ}) is defined by the distance from the jet exit plane to the stagnation point, where the mean axial velocity of the flame is zero. The L_{RZ} for each flame is presented in Table 1. The recirculation zone length for the MB-1 flame is measured to be 91.3 mm. Increasing the fuel jet velocity, and consequently, the jet Reynolds number to 15,000, while the co-flow velocity is kept constant,
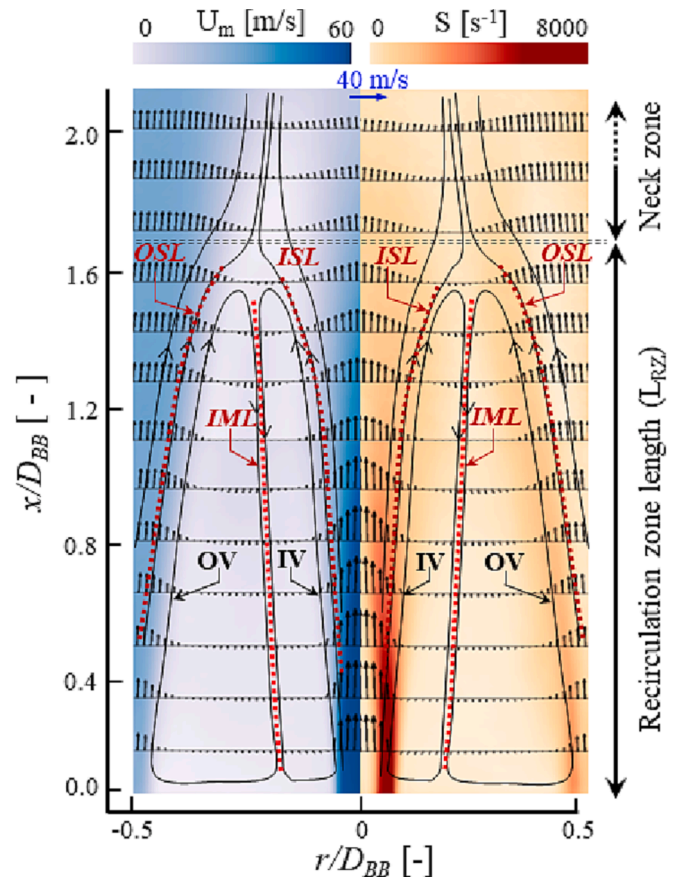

Fig. 4. Ensemble-averaged mean velocity contour (left) and mean strain rate contour (right) overlaid on the vector field and the inner and outer vortices (IV and OV) for a typical methane bluff-body flame (MB-2). The dashed-lines show the inner shear layer (*ISL*), intermediate mixing layer (*IML*) and outer shear layer (*OSL*).

results in an increase in the recirculation zone length by ∼ 15% to 105.1 mm, in MB-2 flame. This is the largest recirculation zone amongst the three flames. In MB-3 flame, where the co-flow air velocity increases to 20 m/s, the recirculation zone length is ∼ 98.8 mm, due to a stronger outer shear layer (*OSL*) leading to an outer vortex restricting the extension of the recirculating upwards. For all three flames, the ratio of the *recirculation zone length* to the *bluff-body diameter* (L_{RZ}/D_{BB}) is 1.42, 1.64, and 1.54 for MB-1, MB-2, and MB-3 flames, respectively. The L_{RZ}/D_{BB} ratio in all three flames is<1.65 which is consistent with earlier investigations in non-premixed bluff-body flames [30], which further shows that mixing and flow dynamics have more significant effects than the heat release on the recirculation zone length. This conclusion is supported by earlier findings of Dally *et al.* [42,43] which characterized the recirculation zone length and mixture strength in reacting and non-reacting flows stabilized on the same bluff-body burner.

3.3. Time-averaged soot volume fraction

3.3.1. Radially-integrated SVF

Fig. 5 presents a collage of the measured time-averaged soot volume fraction (left) for all three flames together with the axial profiles of radially integrated soot volume fraction, in ppm.mm^2 (right). Soot concentrations in the three flames exhibit significant differences in quantity and trends. In MB-1 and MB-3 flames, minimal soot is observed in the recirculation zone, while a distinct peak appears in the jet-like zone. However, in MB-2 flame, two peaks are found; one in the recirculation zone and the other one in the jet-like region. The maximum radially integrated soot in the recirculation zone is 130 ppm.mm^2 for MB-2 flame while it drops to almost 18 to 20 ppm.mm^2 for MB-1 and MB-3 flames. In the jet region, however, the maximum radially-integrated soot in MB-1 flame is around 175 ppm.mm^2 while in the MB-2 and MB-3 flames, it drops to less than a third of the MB-1, (∼50 ppm.mm^2 and 34 ppm.mm^2). Noteworthy is that MB-1 has the lowest jet Reynolds number and air coflow velocity and more fuel burns in the jet-like zone.

Comparing the methane bluff-body flames (MB flames) with ethylene/nitrogen bluff-body flames (ENB flames) [30] as well as the simple jet flames [19,20] reveals that the maximum radially integrated soot volume fraction in the jet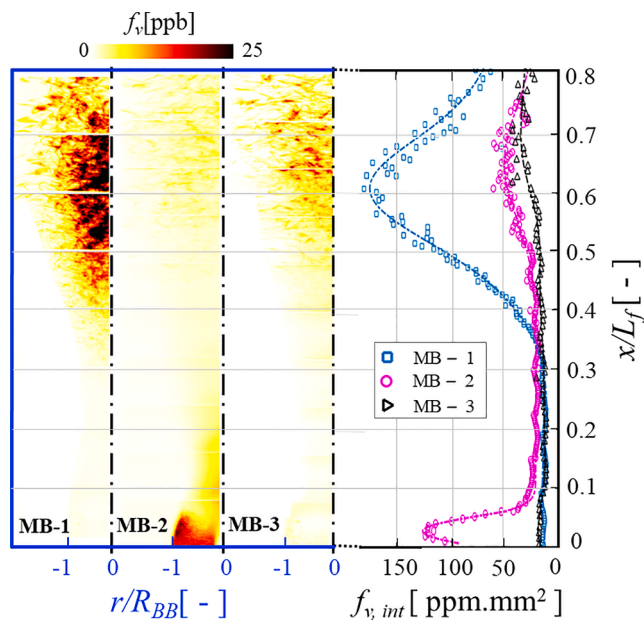 region is found at similar axial location (normalised by the flame length) above the burner of between 0.6 < x/L_f < 0.7. Also noticeable is that while the methane (MB-3) and ethylene/nitrogen flames (ENB-3) are stabilised on the same burner and operating conditions, the maximum radially-integrated soot in the recirculation zone for the MB-3 (∼20 ppm.mm^2) flame is reduced by more than two order of magnitudes, as compared to ENB-3 (∼1000 ppm.mm^2). It is deduced that this difference is related to the difference in the oxidation level and the mean mixture fraction distribution in two flames. This difference is further discussed in Section 3.4.

3.3.2. Axial distribution of SVF

The axial profile of soot volume fraction (*SVF*) at the flame centreline of each flame is presented in Fig. 6. The symbols represent the experimental data, and the dashed lines provide reasonable Gaussian fits. The axial height is normalised by the overall flame length (x/L_f), which enables us to compare the results with the ethylene/nitrogen flame (ENB-3) and the simple jet flames [20].

The *SVF* distribution along the centreline has two distinct peaks in the MB-2 flame: one in the recirculation zone, at $x/L_f = 0.093$, and the other in the jet-like region, found at $x/L_f = 0.59$. This trend is similar to ENB flames. On the other hand, MB-1 and MB-3 flame exhibit only one peak in the jet region. The *SVF* in the jet region peaks to around 17 ppb in the MB-1 flame, which is greater than those in MB-2 and MB-3 flames by a factor of almost three. It is also observed that the peak of *SVF* in MB-2 and MB-3 flames is shifted axially as the Reynolds number is increased in these two flames. The axial location of the maximum *SVF* in the jet region is found to be at $x/L_f = 0.48$, while this location is shifted to x/L_f = 0.59 and 0.63 for MB-2 and MB-3 flames, respectively.

When comparing MB-3 flame with ENB-3 flame [30], noticeable differences are observed. For ENB-3 flame, the axial location of the peak of the SVF profiles on the flame centreline is closer to the upstream region of the flame (at x/ L_f = 0.40), valued at 42 ppb. On the other side, in methane flame (MB-3), the peak is shifted downstream and found at around x/ L_f = 0.63, and the value dropped by a factor of more than eight to around 5 ppb. Interestingly, the peak soot in the methane flame is coincident at a similar position, x/ L_f = 0.60, in the simple jet flames with the same Reynolds number (15,000) [19,20].

3.3.3. Radial distribution of SVF

Fig. 7 compares the mean radial profiles of *SVF* in the recirculation zone for the three flames. The profiles are plotted at four different axial locations above the jet exit plane within the recirculation zone (x/D_{BB} = (0.6, 0.8, 1.2, 1.4). The symbols represent the experimental data. The solid lines were obtained from the best Gaussian fit (with three terms) to the measured data. The bluff-body diameter is used to normalise both axial and radial distances. Consistent with ethylene/nitrogen flames (ENB-1, ENB-2, and ENB-3 flames) [30], a dominant outer peak is found
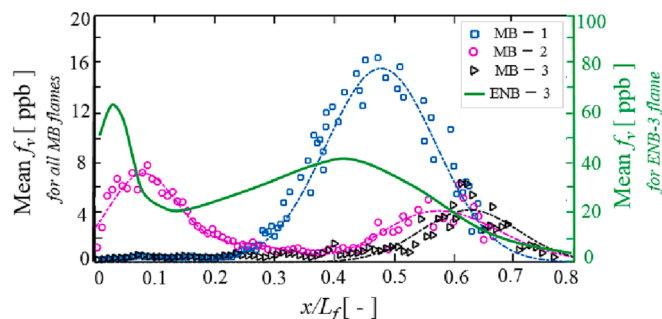
Fig. 5. A collage of the measured time-averaged soot volume fraction (left) for the three flames, together with the axial profiles of radially integrated soot volume fraction, in ppm.mm^2, along the flames' length (right).

Fig. 6. Axial profiles of centreline distribution of mean soot volume fraction as a function of normalised flame length. The dashed lines indicate Gaussian fits to the experimental data. The ENB-3 ethylene/nitrogen bluff-body flame is shown with solid green line from a previous flame series [30]. (For interpretation of the references to colour in this figure legend, the reader is referred to the web version of this article.)
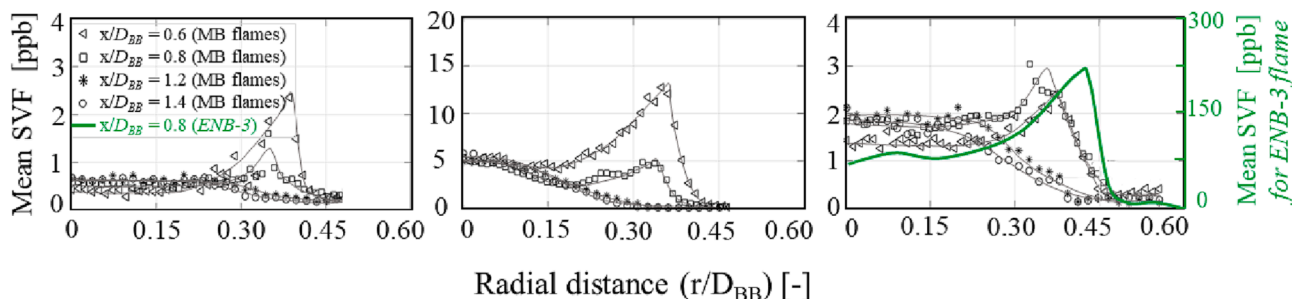
Fig. 7. Radial profiles of mean soot volume fraction of the a) MB-1, b) MB-2, and c) MB-3 flames within the recirculation zone at different heights above the burner (HAB). The ENB-3 ethylene/nitrogen bluff-body flame is shown with solid green line from a previous flame series [30]. (For interpretation of the references to colour in this figure legend, the reader is referred to the web version of this article.)

at $x/D_{BB} < 1$ for all three methane flames near to the coflowing air (inside the outer vortex at $r/D_{BB} \approx 0.35$–0.42) from which it decreases smoothly toward the centreline. An explicit peak is observed at lower axial heights, where the mixture fraction is rich compared with the end of the RZ. At higher locations, x/D_{BB} greater than 1.0, no distinct peak can be identified, and that is believed to be due to the high rate of oxidation due to the intense coflow air entrainment [42,43] and higher temperatures from products leaving the recirculation zone. Such similarities highlight the role of soot transport within the recirculation zone irrespective of the difference in soot inception and chemical effects between the two fuels. The three flames share similar trends in the mean *SVF* profiles, albeit with different peaks.

The radial profiles of mean *SVF* in the jet region ($0.25 < x/L_f < 0.65$) for the three flames are compared in Fig. 8. The heights are normalised by the overall flame length (L_f). The three flames exhibit similar trends showing a maximum for *SVF* on the flame centreline (r = 0 mm), followed by a smooth decrease towards the flame edge, where most of the soot is oxidised. In MB-1 flame, the maximum soot volume fraction SVF_{max} in the jet region is around 22 ppb which is one order of magnitude greater than the maximum *SVF* in the recirculation zone. Similarly, in the MB-3 flame, where the jet and co-flow velocities are maximum among the three flames, the SVF_{max} in the jet region is around 16 ppb which is greater than the SVF_{max} in the RZ by a factor of two to three. Conversely, the MB-2 flame behaves differently. The SVF_{max} in the recirculation zone is found to be around 13 ppb, while a 30% drop in the max *SVF* is observed for this flame in the jet region (7 ppb). Based on this observation in the *SVF* values as well as the flame photos, it is likely that more PAH (or liquid like nascent soot particles) is transported from the recirculation zone to the jet-like region through the neck zone, which initiates the soot inception in the jet region. Also, it is believed that soot inception in the MB-2 flame starts earlier comparing to the other flames, and therefore, there is sufficient time for soot to be formed in the recirculation zone. These observations require further experimental evidence to examine the PAH in the neck zone of the three flames and correlate them with the trends found in these flames. It's worthwhile mentioning that future work is required to measure the PAHs in the recirculation zone and neck zone to identify the nature of the particle

which are transported to the neck and jet regions.

3.3.4. Soot intermittency

Fig. 9 presents the profiles of soot intermittency, defined as the probability of finding no soot at any given spatial location, along with flames centreline [17,20]. The intermittency profiles exhibit two distinct minima for each flame; one in the recirculation zone and a second one in the jet-like region. As expected, at the jet exit, $x/\overline{L}_f = 0$, the intermittency equals 1.0, and then the profile follows a sharp decrease to around 0.32 for MB-1 and MB-3 flames within the recirculation zone. For MB-2 flames, the intermittency reaches < 0.1, consistent with a higher concentration of soot found in the recirculation zone of
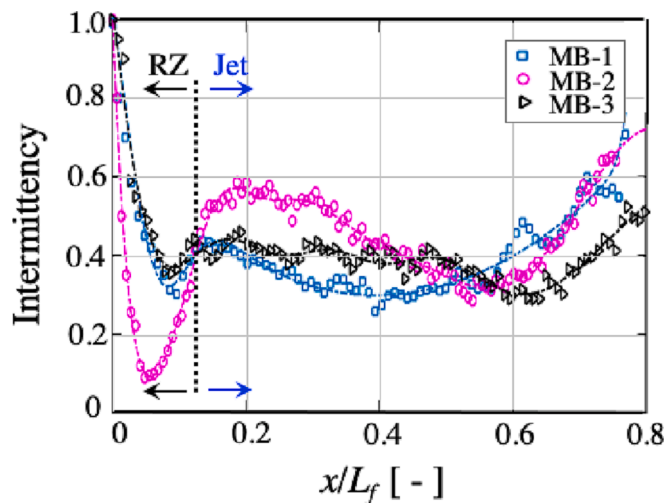

Fig. 9. Axial Profile of soot intermittency along the burner axis. The black arrow specifies the recirculation zone (RZ), and the blue arrows show the jet-like region. (For interpretation of the references to colour in this figure legend, the reader is referred to the web version of this article.)
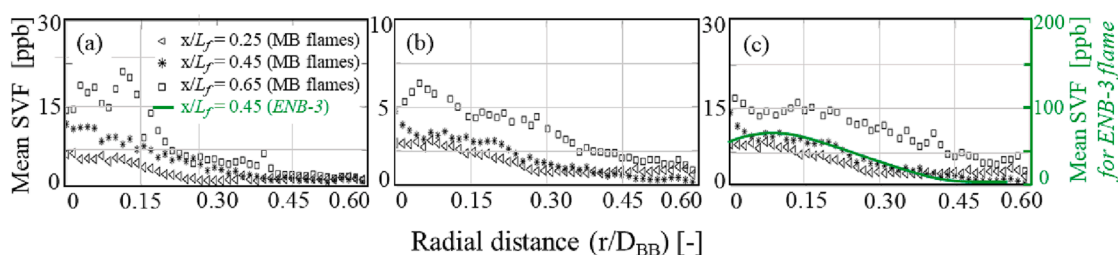

Fig. 8. Radial profiles of mean soot volume fraction a) MB-1, b) MB-2, and c) MB-3 flames in the jet zone at different normalised heights above the burner. Note that the y-axis values differ in each profile. The ENB-3 ethylene/nitrogen bluff-body flame is shown with solid green line from a previous flame series [30]. (For interpretation of the references to colour in this figure legend, the reader is referred to the web version of this article.)

this flame. The sharp decrease observed in the intermittency profile and the SVF measured on the flame centreline highlights the likely effect of transport of soot from the vortices into the central jet and further downstream to the rest of the flame. This observation is based on non-favourable conditions for soot to form at these locations, namely; high strain rate, low temperature and short residence time. At $x/\overline{L}_f \approx 0.12$, it is surprising that the intermittency for all three flames is almost identical at (~ 0.42). This location is identified as the transition from the recirculation zone to the jet-like region.

The minimum intermittency value in the jet region, which corresponds to the maximum axial soot volume fraction on the centreline, is found to be at $x/\overline{L}_f = 0.40, 0.57$, and 0.62 for MB-1, MB-2, and MB-3 flames, respectively. This value for the two MB-1 and MB-2 flames is similar to simple jet flames ($0.38 < x/\overline{L}_f < 0.55$) [20]. However, it is observed that the minimum intermittency in MB-3 is shifted downstream and found at $x/\overline{L}_f \approx 0.62$. Noteworthy is that the difference shown earlier in the appearance and behaviour of soot in MB-2 flame, compared with MB-1 and MB-3 flames, can be explained by the intermittency in the neck zone. It is clear that more soot (and its precursors) is transported through the neck zone in MB-2 flame than the other two flames, leading to a higher amount of soot in the jet-like region.

3.4. Calculated mixture fraction and temperature

In order to better interpret the differences in soot concentration measured in the three flames, the mixture fraction together with the temperature profile is estimated numerically and presented in Fig. 10. The flame temperature and mixture fraction are reported at axial heights of $x/D_{BB} = (0.6, 0.9, 1.2)$, as presented in Fig. 10. It is noted that soot and its impact on thermal radiation from the flame are not computed in this study. The objective is to better understand the differences in flame structure and temperature, rather than to 'predict' soot. The mixture fraction profiles exhibit similar features for the MB-1 and MB-3 flames. That is, a rich mixture is found at almost all locations $r/D_{BB} < 0.42$ and axial height of $x/D_{BB} = 0.6$. However, for MB-2 flame, the mixture fraction profile crosses the stoichiometric value at $r/D_{BB} = 0.24$ at all

heights, suggesting a leaner outer vortex, and a shift of the mean stoichiometric mixture to a distinct location closer to the centreline. The calculated peak mean temperature for the MB-2 flames at the axial height of $x/D_{BB} = 0.6$ is found at $r/D_{BB} \sim 0.19$, within the ISL, at around 1600 K, which is almost 14% lower than those found in the MB-1 and MB-3 flames. The radial location at which the mean temperature peaks are found in MB-1 and MB-3 flames is $r/D_{BB} \sim 0.38$, within the *OSL*, and the computed values are found to be 1880 K and 1870 K, respectively. A similar trend was observed for the calculated OH profile. That is, the OH peak is found at $r/D_{BB} \sim 0.2$ for MB-2 flame, while the peak is shifted toward the *OSL* at $r/D_{BB} \sim 0.39$ for the MB-1 and MB-3 flames. The lower concentration of OH in MB-2 flames is consistent with a lower temperature peak in this flame. Furthermore, a sharp decline is seen in the OH profiles for MB-1 and MB-3, which shows the high rate of oxidation. Notable too is that the calculated OH concentration in MB-1 and MB-3 flames is almost 40% greater than that of MB-2. Although we do not expect that a simplified DRM-22 mechanism may be enough to accurately predict the intermediate species, such as acetylene, it provides trends in the anticipated C_2H_2 concentration in all three cases. In MB-2 flame, the peak of calculated acetylene is almost 40% lower than those of MB-1 and MB-3 flames which again is expected to lead to lower soot, instead of the observed higher soot in MB-2. Based on these observations, it is clear that in MB-2 soot is formed in the inner vortex and then transported to the outer vortex and the partly to the neck region. While in MB-1 and MB-3 the soot is formed in the outer vortex where it has a higher chance to be oxidised and not reach the central jet and the neck zone. The trend found in section 3.3.3, where higher soot in the recirculation zone is recorded in MB-2, while is inconsistent with the lower temperature, and lower C_2H_2 found there, is consistent with the lower oxidation rate expected in the rich inner vortex. Worth noting is that the photographs of the flames, presented in Fig. 2, while showing faint soot in the recirculation zone of MB-1 and MB-3 flames, are long-term exposure images and the blue colour from regions of the flame does not necessarily imply the absence of soot.
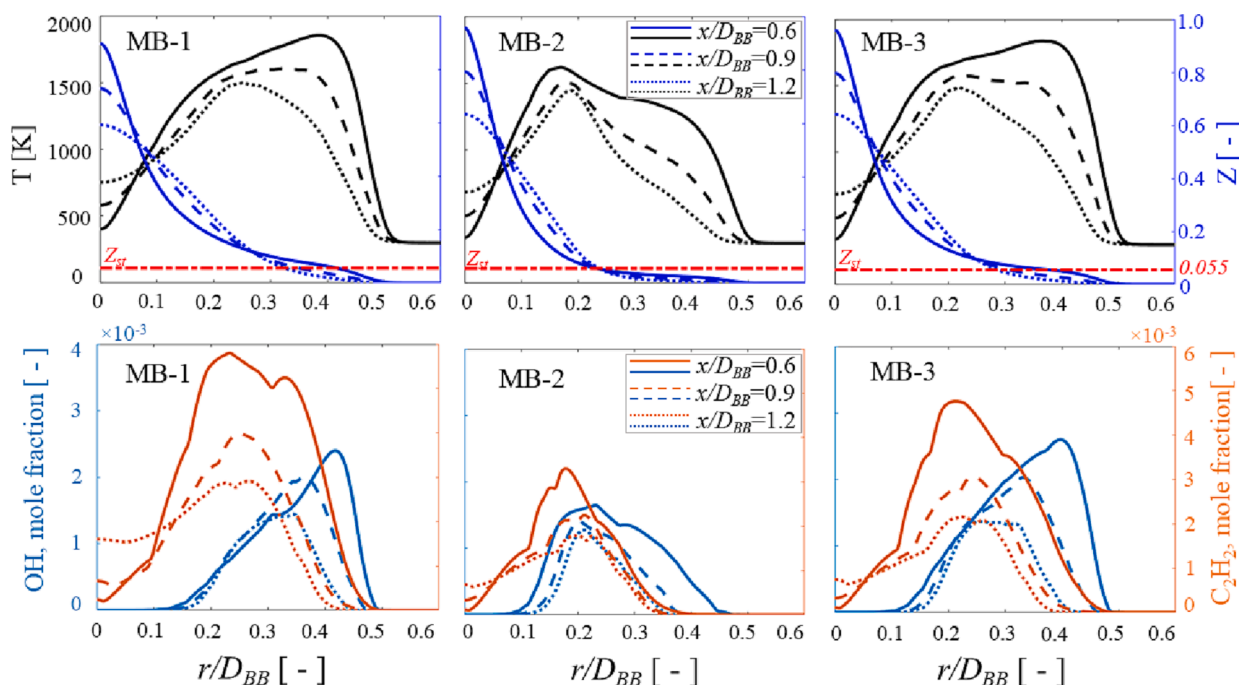

Fig. 10. Calculated mean radial profile of temperature and mixture fraction (top row) together with the OH and acetylene mole fraction (bottom row) for the three flames and at three axial locations. The dashed red line indicates the stoichiometric mixture fraction. (For interpretation of the references to colour in this figure legend, the reader is referred to the web version of this article.)

3.5. Relations between instantaneous soot and strain rate

Fig. 11 presents a typical instantaneous P-LII soot sheet from a methane flame (MB-3) on the *RHS* and another from the ethylene/nitrogen flame (ENB-3) on the *LHS*. As noted earlier, these two flames run under identical operating conditions. Although the flowfield behaves similarly for both fuels, the soot distribution is different. In the ENB-3 flame, soot filaments are chaotic and found almost in the entire recirculation zone length, whilst in the MB-3 flame, the soot filaments are more concentrated in the outer shear layer close to the outer flame edge and rarely in the inner vortex. The maximum instantaneous soot in methane is almost one order of magnitude lower than the ethylene/nitrogen (ENB-3) flame. Given that the mixing is similar for the two flames, it is evident that differences in fuel composition and subsequent reaction chemistry are dominant and appears to impact the formation and growth of soot particulates.

Fig. 12 presents a typical instantaneous radial profile of *SVF* and strain rate at one axial height above the burner ($x/D_{BB} = 0.6$) for the three flames. The *SVF* and strain rate are shown in orange and blue colours, respectively.

It is clear from this figure that the local instantaneous *SVF* and *S* peak at the inner and outer locations while showing a plateau distribution in the middle of the profiles. A noticeable amount of soot is found in the low-strain region ($S < 5000 \text{ s}^{-1}$) with a soot concentration of 10 ppb. In contrast, in MB-2 flame, a peak of ≈ 30 ppb is observed at $r/D_{BB} = 0.38$ at the same strain rate compared to the other two flames. The lack of direct correlation between the instantaneous soot volume fraction, PAH and instantaneous strain provides further evidence of the impact of transport in the recirculation zone. Future work is required to investigate the instantaneous correlations between the soot volume fraction and PAH to instantaneous strain rate.
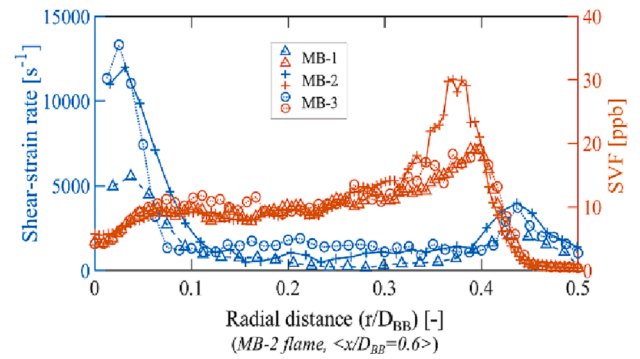

Fig. 12. Profiles of instantaneous *SVF* and *S* at the axial height of $x/D_{BB} = 0.6$ above the burner for all flames.

3.6. Soot statistics

The probability density functions (PDFs) of *SVF* have been calculated in the recirculation zone of the three flames. The axial and radial positions at which the PDFs have been calculated are shown in Fig. 13. The PDFs were calculated from arrays of 5×5 pixels^2 (0.17 mm^2) from 1500 instantaneous image pairs. The data used are from two axial heights above the burner within the recirculation zone ($x/D_{BB} = 0.6, 1.0$) and at three radial positions, two of which are on the high-strain inner and outer shear layers (*ISL* and *OSL*), and the third one is in the core of the recirculation zone between the *ISL* and the *OSL*.

Fig. 14 presents the PDFs of the *SVF* at $x/D_{BB} = 0.6$ and $x/D_{BB} = 1.0$. The shapes of the PDFs indicate different soot concentrations for the three flames. The width of the pdfs for the MB-2 flames is significantly broader than the other two flames, which is believed to be the oxidation effects, while only a peak following a sharp decrease is seen in MB-1 and
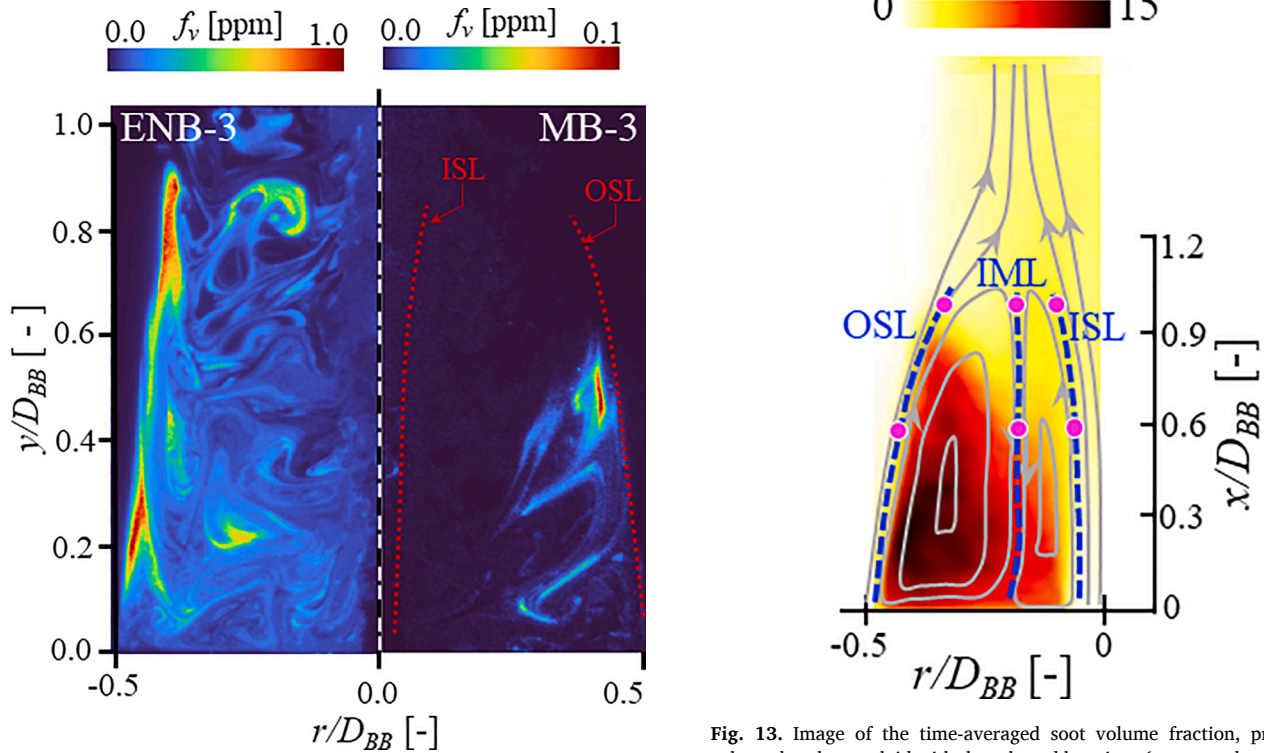

Fig. 11. Comparison of a typical instantaneous soot filament of the (LHS) ENB-3 [30] and (RHS) MB-3 flame. Note that the colour bars scale differently for two flames. Dotted lines indicated the inner (ISL) and outer (OSL) shear layers.

Fig. 13. Image of the time-averaged soot volume fraction, presented as a coloured-scale, overlaid with the selected locations (magenta dots) at which the statistics for SVF have been calculated for the MB-2 flame adopted from earlier work [29]. (For interpretation of the references to colour in this figure legend, the reader is referred to the web version of this article.)
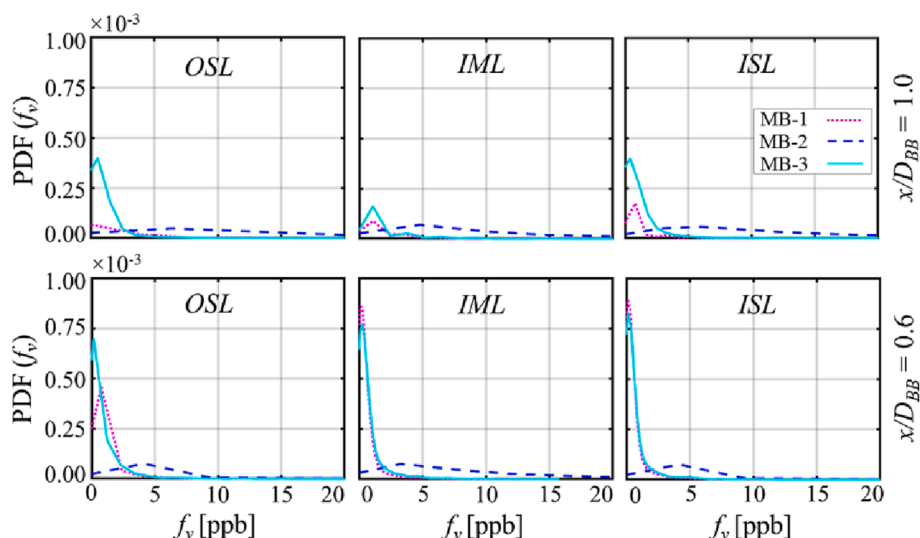
Fig.14. Axial distribution of probability density functions (PDFs) of soot volume fraction within the recirculation zone at a series of radial locations and at two axial locations above the burner $x/D_{BB} = 0.6$ (bottom row) and $x/D_{BB} = 1.0$ (top row).

MB-3 flames. While the probability of finding soot in the MB-1 is the least, increasing the Reynolds number to 15,000 (MB-2) increases the maximum probable soot to 7 ppb. For the MB-2 flame, no events higher than 25 ppb are found.

In contrast, in MB-1 and MB-3 flames, the maximum probable soot is reduced by a factor of more than two, to<10 ppb. This is consistent with the total soot calculated for the recirculation zone of each flame in Fig. 5. It is also deduced that the effect of soot oxidation is significant at lower momentum flux ratio. Noting that the MB-2 flame has the higher momentum flux ratio amongst the three flames, it can be deduced that the lower momentum flux ratio correlates with higher soot oxidation and less probability of having soot in a specific region.

4. Conclusions

A joint experimental and computational work was performed to investigate the soot formation and oxidation in a series of turbulent non-premixed bluff-body flames burning pure methane. Simultaneous planar laser-induced incandescence (P-LII) and 2D polarised particle image velocimetry (P-PIV) techniques have been employed to measure soot and flowfield features, respectively. Three flames stabilised on the 4.6 mm fuel jet and 64 mm bluff body diameters burner using a combination of the jet Reynolds number, 8,000 and 15,000, and co-flowing air velocity, 14 m/s and 20 m/s are presented in this paper.

Although all flames exhibit similar features, namely two vortices within the recirculation zone, a significant increase is observed in the mean *SVF* and the soot intermittency profiles for the MB-2 flame. The difference mainly arises from the mixture fraction distribution resulting in a mean stoichiometric mixture in the inner vortex, closer to the jet, in MB-2, while for the MB-1 and MB-3 flames a broader distribution of the mixture fraction is found in the outer vortex. This difference results in less soot concentration in the MB-1 and MB-3 flames as compared with MB-2. Also, the leaner mixture fraction in the inner recirculation zone for the MB-1 and MB-3 flames results in less soot being formed and a higher probability of it being oxidised in the neck zone.

The total integrated soot exhibited two maxima in the recirculation zone of the MB-2 flame versus one peak in the other two flames. This difference could be attributed to the mean mixture fraction in the recirculation zone of MB-2 flame, which is relatively higher than those in MB-1 and MB-3 flames considering the similar mean residence time within this region. All soot events were found to be in the range of 1 ppb < *SVF* < 6 ppb in the MB-1 and MB-3 flame, while a uniform SVF distribution is observed for the MB-2 flame with the maximum number of events found in the range 1 ppb < *SVF* < 25 ppb. It is observed that although the maximum local instantaneous soot is around 25 ppb, the time-averaged soot is<10 ppb which could be related to the high soot intermittency and turbulence fluctuations. The soot and flowfield data presented in this work are expected to be useful for further model validations and development.

CRediT authorship contribution statement

Amir Rowhani: Conceptualization, Methodology, Investigation, Formal analysis, Writing – original draft. **Zhiwei Sun:** Methodology, Investigation. **Alfonso Chinnici:** Investigation. **Paul R. Medwell:** Writing – review & editing, Supervision. **Graham J. Nathan:** Writing – review & editing, Supervision. **Bassam B. Dally:** Conceptualization, Formal analysis, Writing – review & editing, Supervision.

Declaration of Competing Interest

The authors declare that they have no known competing financial interests or personal relationships that could have appeared to influence the work reported in this paper.

Data availability

Once the paper is accepted, the data will be published on the "international sooting flame workshop - ISF"

Appendix A. Supplementary data

Supplementary data to this article can be found online at https://doi.org/10.1016/j.fuel.2023.128118.

References

[1] Castaldi MJ, Marinov NM, Melius CF, Huang J, Senkan SM, Pitz WJ, et al. Experimental and modeling investigation of aromatic and polycyclic aromatic

hydrocarbon formation in a premixed ethylene flame. Proc Combust Inst 1996;26:693–702.

[2] Smooke MD, Hall RJ, Colket MB, Fielding J, Long MB, McEnally CS, et al. Investigation of the transition from lightly sooting towards heavily sooting co-flow ethylene diffusion flames. Combust Theo Model 2004;8:593–606.

[3] Michelson HA, Colket MB, Bengtsson PE, D'Anna A, Desgroux P, Haynes BS, et al. A Review of Terminology Used to Describe Soot Formation and Evolution under Combustion and Pyrolytic Conditions. ACS Nano 2020;14:12470–90.

[4] Agosta A, Boccara G, Coughlan H, Heringa B, Browne N, Dediu D. Global Gas Outlook to 2050, https://www.mckinsey.com/industries/oil-and-gas/our-insights/global-gas-outlook-to-2050.

[5] Calcote HF, Manos DM. Effect of Molecular Structure on Incipient Soot Formation. Combust Flame 1983;49:289–304.

[6] Schug KP, Manheimer-Timnat Y, Yaccarino P, Glassman I. Sooting Behavior of Gaseous Hydrocarbon Diffusion Flames and the Influence of Additives. Combust Sci Technol 1980;22:235–50.

[7] Cuoci A, Frassoldati A, Faravelli T, Ranzi E. Formation of soot and nitrogen oxides in unsteady counterflow diffusion flames. Combust Flame 2009;156:2010–22.

[8] Cuoci A, Frassoldati A, Faravelli T, Ranzi E. Soot formation in unsteady counterflow diffusion flames. Proc Combust Inst 2009;32:1335–42.

[9] Chernov V, Thomson MJ, Dworkin SB, Slavinskaya NA, Riedel U. Soot formation with C1 and C2 fuels using an improved chemical mechanism for PAH growth. Combust Flame 2014;161:592–601.

[10] Liu S, Chan TL, He Z, Lu Y, Jiang X, Wei F. Soot formation and evolution characteristics in premixed methane/ethylene-oxygen-argon burner-stabilised stagnation flames. Fuel 2019;242:871–82.

[11] Gülder ÖL, Intasopa G, Joo HI, Mandatori PM, Bento DS, Vaillancourt ME. Unified behaviour of maximum soot yields of methane, ethane and propane laminar diffusion flames at high pressures. Combust Flame 2011;158:2037–44.

[12] Christopher CR, Williams TC. The effect of oxygen enrichment on soot formation and thermal radiation in turbulent, non-premixed methane flames. Proc Combust Inst 2017;36:4051–9.

[13] Shaddix CR, Zhang J, Williams TC. Soot Concentration, Temperature, and Radiant Emission Measurements in a Turbulent Ethylene Jet Flame. presented at the 11th USS National Combustion Meeting, Pasadana, California, 2019.

[14] Desgroux P, Faccinetto A, Mercier X, Mouton T, Karkar DA, Bakali AE. Comparative study of the soot formation process in a "nucleation" and a "sooting" low pressure premixed methane flame. Combust Flame 2017;184:153–66.

[15] Wang Y, Chung SH. Soot formation in laminar counterflow flames. Prog Energy Combust Sci 2019;74:152–238.

[16] Wang Y, Gu M, Wu J, Cao L, Lin Y, Huang X. Formation of soot particles in methane and ethylene combustion: A reactive molecular dynamics study. Int J Hydrog Energy 2021. https://doi.org/10.1016/j.ijhydene.2021.08.125.

[17] Qamar NH, Nathan GJ, Alwahabi ZT, King KD. The effect of global mixing on soot volume fraction: measurements in simple jet, precessing jet, and bluff body flames. Proc Combust Inst 2005;30:1493–500.

[18] Qamar NH, Alwahabi ZT, Chan QN, Nathan GJ, Roekaerts D, KingKD. Soot volume fraction in a piloted turbulent jet non-premixed flame of natural gas. Combust Flame 2009;156:1339–47.

[19] Mahmoud SM, Nathan GJ, Alwahabi ZT, Sun ZW, Medwell PR, Dally BB. The effect of exit Reynolds number on soot volume fraction in turbulent non-premixed jet flames. Combust Flame 2018;187:42–51.

[20] Mahmoud SM, Nathan GJ, Alwahabi ZT, Sun ZW, Medwell PR, Dally BB. The effect of exit strain rate on soot volume fraction in turbulent non-premixed jet flames. Proc Combust Inst 2017;36:889–97.

[21] Mahmoud SM, Nathan GJ, Medwell PR, Dally BB, Alwahabi ZT. Simultaneous planar measurements of temperature and soot volume fraction in a turbulent non-premixed jet flame. Proc Combust Inst 2015;35:1931–8.

[22] Köhler M, Geigle KP, Blacha T, Gerlinger P, Meier W. Experimental characterisation and numerical simulation of a sooting lifted turbulent jet diffusion flame. Combust Flame 2012;159:2620–35.

[23] Köhler M, Boxx I, Geigle KP, Meier W. Simultaneous planar measurements of soot structure and velocity fields in a turbulent lifted jet flame at 3 kHz. Appl Phys B 2011;103:271–9.

[24] Köhler M, Geigle KP, Meier W, Crosland BM, Thomson KA, Smallwood GJ. Sooting turbulent jet flame: characterisation and quantitative soot measurements. Appl Phys B 2011;104:409–25.

[25] Mueller ME, Chan QN, Qamar NH, Dally BB, Pitsch H, Alwahabi ZT. Experimental and computational study of soot evolution in a turbulent non-premixed bluff body ethylene flame. Combust Flame 2013;160:1298–309.

[26] Deng S, Mueller ME, Chan QN, Qamar NH, Dally BB, Alwahabi ZT. Hydrodynamic and chemical effects of hydrogen addition on soot evolution in turbulent non-premixed bluff- body ethylene flames. Proc Combust Inst 2017;36:807–14.

[27] Geigle KP, Köhler M, O'Loughlin W, Meier W. Investigation of soot formation in pressurised swirl flames by laser measurements of temperature, flame structures and soot concentrations. Proc Combust Inst 2015;35:3373–80.

[28] Chatterjee S, Gülder ÖL. Soot concentration and primary particle size in swirl-stabilised non-premixed turbulent flames of ethylene and air. Exp Therm Fluid Sci 2009;95:73–80.

[29] Wang LY, Bauer CK, Gülder ÖL. Soot and flow field in turbulent swirl-stabilised spray flames of Jet A-1 in a model combustor. Proc Combust Inst 2019;37:5437–44.

[30] Rowhani A, Sun ZW, Medwell PR, Nathan GJ, Dally BB. Soot-flowfield interactions in turbulent non-premixed bluff-body flames of ethylene/nitrogen. Proc Combust Inst 2021;38:1125–32.

[31] Rowhani A, Sun ZW, Medwell PR, Nathan GJ, Dally BB. Relationships between Soot and the local instantaneous strain rate in turbulent non-premixed bluff-body flames. Energy Fuels 2022;36:12181–91.

[32] Rowhani A, Sun ZW, Medwell PR, Alwahabi ZT, Nathan GJ, Dally BB. Effects of the bluff-body diameter on the flow field characteristics of non-premixed turbulent highly-sooting flames. Combust Sci Technol 2019;194:378–96.

[33] Schulz C, Kock BF, Hofmann M, Michelsen H, Will S, Bougie B, et al. Laser-induced incandescence: recent trends and current questions. Appl Phys B 2006;83:336–54.

[34] International Sooting Flame (ISF) Workshop (2021). http://www.adelaide.edu.au/cet/isfworkshop/ (accessed 23 July 2016).

[35] Sun ZW, Alwahabi ZT, Gu DH, Mahmoud SM, Nathan GJ, Dally BB. Planar laser-induced incandescence of turbulent sooting flames: the influence of beam steering and signal trapping. Appl Phys B 2015;119:731–43.

[36] Kruse S, Medwell PR, Beeckmann J, Pitsch H. The significance of beam steering on laser-induced incandescence measurements in laminar counterflow flames. Appl Phys B 2018;124:212.

[37] Rowhani A, Chennici A, Evans MJ, Medwell PR, Nathan GJ, Dally BB. Variation of residence time in non-premixed turbulent bluff-body ethylene flames as a function of burner diameter. 21st Australasian Fluid Mechanics Conference, Adelaide, Australia, 2018.

[38] Thielicke W, Stamhuis EJ. PIVlab - Towards User-friendly, Affordable and accurate digital particle image velocimetry. J Open Res Soft 2014:2.

[39] Thielicke W. The flapping flight of birds - analysis and application. Rijksuniversity Groningen 2014:1–10.

[40] ANSYS® Fluent, Release 21.1.

[41] Dally BB, Masri AR. Modelling of Bluff-body recirculating flows, 12st Australasian Fluid Mechanics Conference. Sydney: Australia; 1995.

[42] Dally BB, Fletcher DF, Masri AR. Flow and mixing fields of turbulent bluff-body jets and flames. Combust Theor Model 1998;2:193–219.

[43] Dally BB, Masri AR, Barlow RS, Fiechtner GJ. Instantaneous and Mean Compositional Structure of Bluff-Body Stabilized Nonpremixed flames. Combust Flame 1998;114:119–48.